Substrate constraint modifies the Rayleigh spectrum of vibrating sessile drops

Chun-Ti Chang,[1] Joshua B. Bostwick,[2] Paul H. Steen,[1,3,*] and Susan Daniel[1,3,†]
[1]*Theoretical and Applied Mechanics, Cornell University, Ithaca, New York 14853, USA*
[2]*Department of Mathematics, North Carolina State University, Rayleigh, North Carolina 27695, USA*
[3]*School of Chemical and Biomolecular Engineering, Cornell University, Ithaca, New York 14853, USA*
(Received 9 April 2013; published 14 August 2013)

In this work, we study the resonance behavior of mechanically oscillated, sessile water drops. By mechanically oscillating sessile drops vertically and within prescribed ranges of frequencies and amplitudes, a rich collection of resonance modes are observed and their dynamics subsequently investigated. We first present our method of identifying each mode uniquely, through association with spherical harmonics and according to their geometric patterns. Next, we compare our measured resonance frequencies of drops to theoretical predictions using both the classical theory of Lord Rayleigh and Lamb for free, oscillating drops, and a prediction by Bostwick and Steen that explicitly considers the effect of the solid substrate on drop dynamics. Finally, we report observations and analysis of drop mode mixing, or the simultaneous coexistence of multiple mode shapes within the resonating sessile drop driven by one sinusoidal signal of a single frequency. The dynamic response of a deformable liquid drop constrained by the substrate it is in contact with is of interest in a number of applications, such as drop atomization and ink jet printing, switchable electronically controlled capillary adhesion, optical microlens devices, as well as digital microfluidic applications where control of droplet motion is induced by means of a harmonically driven substrate.

DOI: 10.1103/PhysRevE.88.023015 PACS number(s): 47.20.Ma, 47.55.dr

I. INTRODUCTION

The dynamics of an oscillating free drop was predicted by Lord Rayleigh [1]. This early work took account of surface tension and inertia in the case where viscous effects are negligible, as appropriate for water drops on the millimeter scale. Rayleigh characterized the dynamics of a plucked, freely oscillating, spherical drop by its natural frequencies:

$$\omega_n^2 = \frac{\sigma}{\rho R^3} n(n-1)(n+2), \quad n = 0,1,2,\ldots, \tag{1}$$

where σ is the surface tension, R is the radius of the undisturbed drop, and ρ is the density of the drop fluid. Corresponding drop mode shapes have radial deformations that are given by the Legendre polynomials $P_n(\cos(\theta))$, a subset of the spherical harmonics (solutions of the Laplace equation in three dimensions), where θ is the angle to the north pole in a spherical coordinate system [2,3]. Note that these shapes are axisymmetric. We shall refer to mode shapes P_n with frequencies ω_n as "Rayleigh drops." Rayleigh's predictions have been verified experimentally for immiscible drops by Trinh and Wang [4] and for free drops in microgravity by Wang, Anilkumar, and Lee [5], both using acoustic excitation. Rayleigh's prediction for the oscillating free drop still sees widespread use even in situations where the drop is not completely free, as for a drop levitated [6,7] or in contact with a solid [8–12] or with another liquid [13]. Modifications, *ad hoc* or otherwise, to Eq. (1) are often invoked to account for the influence of substrate contact on drop frequency [14–16]. Why has Rayleigh's result proved to be so resilient and what are its limits of applicability in the sessile drop case? This is the focus of our paper.

A sessile drop is a drop that sits on a planar substrate. For sessile drops both the equilibrium contact angle and the mobility of the contact line will influence frequencies and mode shapes. A subset of Rayleigh drops are exact solutions for sessile drops under the right conditions. This is because even modes (n = even) have a zero normal velocity on the equatorial plane and thereby automatically satisfy the no penetration condition. Hence, provided the contact-line motion of the sessile drop is not restricted (i.e., is mobile) and the equilibrium shape is hemispherical (i.e., has a 90° contact angle), the Rayleigh half-drop is a solution to the sessile drop governing equations. These solutions will be called "Rayleigh half-drops" and, along with their frequencies, constitute the Rayleigh spectrum. They are illustrated in the first row of Fig. 1 ($l = 0$ modes).

There are other solutions to the linear stability equations that the Rayleigh drops solve, as noted by Lamb [2] and others [17]. These solutions are also spherical harmonics, but include shapes that break the axisymmetry of the Rayleigh drops:

$$r(\theta,\psi) = 1 + \varepsilon P_k^l(\cos\theta)\cos(l\psi), \quad 0 \leqslant \theta \leqslant \pi, \quad 0 \leqslant \psi \leqslant 2\pi. \tag{2}$$

Here r is the scaled radial coordinate and θ and ψ are polar and azimuthal angles in spherical coordinates, ε is the magnitude of deformation such that $\varepsilon \ll 1$, and $P^l{}_k$ is the associated Legendre function of degree k and order l. The axisymmetric Rayleigh half-drops are zonal modes in the spherical harmonic classification, corresponding to $l = 0$ with mode shapes $P_n = P_n^0$, as noted above. The shapes of Eq. (2) have frequencies given by Eq. (1), which makes them degenerate eigenmodes. We shall refer to these modes and frequencies as the "Lamb spectrum." For Lamb modes, the condition $k + l =$ even guarantees no penetration on the equatorial plane and, hence, provides nonzonal solutions to the sessile drop equations, again for hemispherical drops

*Corresponding author: phs7@cornell.edu
†Corresponding author: sd386@cornell.edu

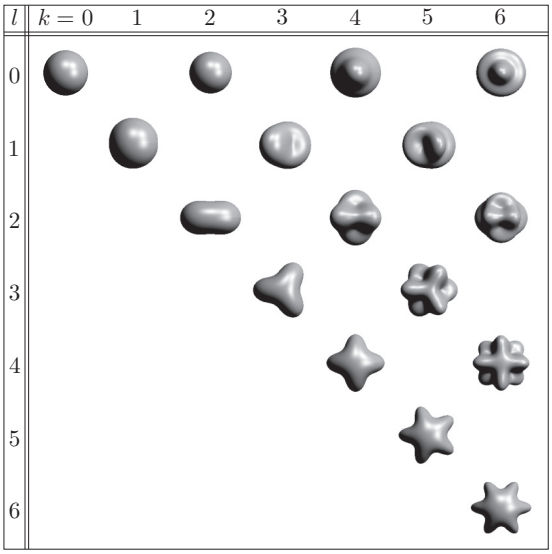

FIG. 1. Eigenmodes of hemispherical drops predicted by the theory of Rayleigh and Lamb are spherical harmonics. Zonal modes are in row 1 ($l = 0$), sectoral modes are along the diagonal ($k = l$), and tesseral modes are where $k \neq l$. Note that the shape at (0,0) is the static drop shape.

with mobile contact lines. We will refer to these as "Lamb half-drops." These are illustrated in Fig. 1 in the rows below row one. The gaps in Fig. 1 represent the missing spherical harmonic solutions ($k + l =$ odd). Nonzonal modes ($l \neq 0$) are called "sectoral" if $k = l$, and "tesseral" if $k \neq l$. In Fig. 1, zonal modes occupy row one, sectoral modes fall on the diagonal, and the tesseral modes are all others. The (0,0) entry is the static equilibrium spherical-cap shape.

For Lamb half-drop solutions, it turns out that nonzonals have identical frequencies to the corresponding zonal mode, according to the modal degeneracy. That is, all modes with the same k have the same frequency. To excite nonzonals in experiments with free drops, the source of excitement must break the symmetry by some means. For example, Shen *et al.* [18] have reported sectoral free drop oscillations excited using ultrasound. They employ a modulated time-periodic driving signal. The base signal (higher frequency) biases the drop to a prolate shape and the superimposed modulation (lower frequency) induces the sectoral shape. Sectorals up to seventh order are reported (up to $k = l = 7$) and, with a simple adjustment, observed frequencies compare reasonably to Lamb's sectoral predictions. For other levitation methods, using various excitation techniques, only zonal modes have been reported [6,15]. Tesseral modes have never been reported for levitated drop experiments, as far as we are aware, although the large-amplitude shapes reported in the free fall experiments of Azuma and Yoshihara [19] may have started from tesserals. Even for levitated drops, the levitating force can influence the spectrum, as has been reported for diamagnetic levitation [6].

Drop contact with a solid has long been recognized to modify the Rayleigh spectrum. Strani and Sabetta [8,20] studied drops in contact with a solid support of spherical bowl shape. Studies were restricted to axisymmetric shapes and predicted frequencies of vibration compared favorably to experiment [4,21,22]. More recently, Bostwick and Steen have reported the spectrum for a drop constrained by a spherical belt support [23,24]. This two-parameter family of constraint recovers as special cases the Strani and Sabetta spectrum and that for a drop pinned along a circle, also considered elsewhere [25,26]. Strani and Sabetta's spherical bowl results were pressed into service to account for the influence on frequency of the constraint of a planar substrate, with some success, at least for nonwetting drops [27]. Smithwick and Boulet's measurements of a vibrating mercury drop on a glass plate showed zonal shapes with a frequency response at half the driving frequency [27]. A subharmonic response was also noted by Yoshiyasu *et al.*, who studied gravity-distorted nonwetting sessile drops, driven by a plane-normal substrate oscillation [14]. They reported sectoral-like shapes. Chebel *et al.* subjected a buoyant drop, attached to a capillary and immersed in a water bath, to volume oscillations [12]. They report a frequency response that matches the Rayleigh spectrum to within 3% for the first three zonal modes, even though the buoyancy considerably distorts the static shape. Ganan and Barerro [28] compares measured frequencies against predictions from their spectral-based computation to find agreement to 4% for vibrating pinned drop modes that include several tesseral shapes. Brunet and Snoeijer vibrate drops on hydrophobic surfaces (contact angle 140°) and observe starlike, tesseral modes as the acceleration of the surface increases [7]. They note a chaotic regime where the coexistence between two or several modes leads to an undefined (or fluctuating) number of nodes just before drop breakup.

The literature on driven sessile drops is large and growing; we have restricted our review of the literature to focus on previous work most relevant to this experimental study. More recently, the dynamics of the three-phase contact line has been a focus of theoretical efforts [29–31]. Lyubimov *et al.* [30] restricts to axisymmetric oscillations of a hemispherical drop, allowing contact-line movement by a Hocking condition. A related analysis of asymmetric disturbances considers both plate-normal and plate-tangential driving forces [29]. The analysis of Fayzrakhmanova and Straube [31] also restricts to hemispherical drops and axisymmetric disturbances, where here the new feature is that a stick-slip Hocking condition has been implemented. Modifications of the Rayleigh spectrum are reported in these three studies. Noblin *et al.* vertically vibrated sessile drops exhibiting moderate contact angle hysteresis (10°–15°) and studied the transition from pinned to slipping contact line, the stick-slip regime [32]. These studies showed that the transition between regimes occurs when the contact angle fluctuation during vibration exceeds the contact angle hysteresis. Comparison of stick-slip behavior is also conducted in experiments that use white noise vibration to excite multiple resonance modes of sessile water drops on either a hydrophobic polystyrene surface (no slip), or superhydrophobic pillared surface (with significant slip) [33]. These experiments demonstrate that resonance frequencies decrease with contact angle and that contact-line slipping impacts (dampens) the higher frequency modes more than the lower ones. In a more recent follow-up study of water drops on a hydrophobic substrate driven by plane-normal oscillations, Noblin *et al.* observe sectoral shapes up to $l = 3$ and report

that contact-line mobility is a necessary condition for these to appear [34]. When the contact line is pinned, at lower driving amplitudes, only zonal modes are seen. A model that uses the one-dimensional dispersion relationship for gravity-capillary waves on a liquid bath of finite depth is proposed to account for these frequencies. Sharp *et al*. test Noblin's model by measuring frequencies of nonzonal drops over a range of contact angles and find qualitatively similar dependence but quantitative discrepancies on the order of 20% [16].

Another recent focus of experimental studies of sessile drops is the "rocking mode" [9,35], an asymmetric mode, excitable by either in-plane or plane-normal driving oscillations, which seems to be linked to droplet translation [11,13,36]. Brunet *et al*. induce droplets to move uphill [36]. Noblin *et al*. use a combination of in-plane and plane-normal driving oscillations to induce droplets to move laterally [11]. Dorbolo *et al*. bounce an oil drop on a vibrating oil-air interface and report observed shapes using a spherical harmonics classification [13]. They point out an asymmetric shape $(k,l) = (2,1)$ that, when excited, "rolls on the vibrated surface without touching it." Finally, Vuvvkasinovic *et al*. drive a sessile water drop with a piezoelectric actuator and document the wave patterns corresponding to resonance frequencies on increasing driving amplitude until the drop is atomized [37]. On driving harder, they report the following sequence of waves: axisymmetric standing, azimuthal standing, azimuthal rotating, a "lattice mode," preejection waves, and finally atomized breakup. Along the way, 14 zonals are reported and several nonzonals, by making the association via dominant wave numbers. Their nonzonal modes may well be mixtures between more than one pure mode as the transitions in wave numbers are gradual. Their zonals have pinned contact lines and respond harmonically to the driving signal. The nonzonals respond subharmonically, consistent with other literature reports. However, in contrast to the Noblin observation, contact-line motion is believed to coincide with the appearance of nonzonal modes, not to precede it.

In our experimental study, symmetry is broken by the substrate plane and by the nonmobile contact-line behavior. However, because disturbed drop shapes satisfy periodicity in the azimuthal direction, the spherical harmonic classification into zonal, sectoral, and tesseral shapes still holds. Strictly speaking, since the shapes are modified from those for the Lamb half-drops, these are "zonal-like," "sectoral-like," and "tesseral-like" modes. However, for simplicity, we will drop the "like" in what follows. We demonstrate the utility of this classification by showing how zonal, sectoral, and tesseral shapes can be identified. In particular, we report observation of the first 36 modes, which includes zonals up to $k = 14$, and sectorals up to $k = l = 10$, with the balance being tesserals [save for one mode $(k,l) = (10,4)$]. Observed modes are summarized in Fig. 5. We then turn to the observed frequency of oscillation. It turns out that zonals respond harmonically to the driving frequency, while nonzonals respond subharmonically. Frequencies are then compared against those of the Rayleigh drop, Eq. (1), and against those predicted by a recent solution of the governing equations by Bostwick and Steen for an inviscid sessile drop of contact angle α and pinned contact line, to be presented elsewhere. The predictions of Bostwick and Steen do better than Rayleigh and Lamb. Finally, we report that mode mixing often occurs, another manifestation of nonlinearity. Linear theory predictions are useful nevertheless.

II. EXPERIMENTAL RESULTS

A. Imaging system

In experiments, the mechanical oscillation signal is generated by an Agilent 33220A function generator (Agilent Technologies, Santa Clara, CA), amplified by a Crown CE2000 power amplifier (Crown Audio, Elkhart, IN), and finally sent to a VTS-100 mechanical vibrator (Vibration Testing Systems, Aurora, OH). A RedLake HG-XL high-speed camera (DEL Imaging Systems, Cheshire, CT) captures images of sessile drops. The optics used on the camera are a Sigma 180 F2.8 APO Macro lens and Vitacon 2X AUTO Teleconverter (NIF). An observation platform is capable of providing top, left or right view, one at a time of an oscillating drop through integration of multiple mirrors (BB1-E02 Broadband Dielectric Mirrors, by Thorlabs, Newton, NJ). A schematic of the integrated hardware system is shown in Fig. 2. For each image set of a given condition, 200 sequential frames were recorded. Further details on the resolution of imaging can be found in the Appendix.

A key aspect of our system that enables identification of higher drop modes is a platform that allows collection of two-dimensional spatial drop deformation by top-view imaging. Drops are placed on chemically functionalized glass

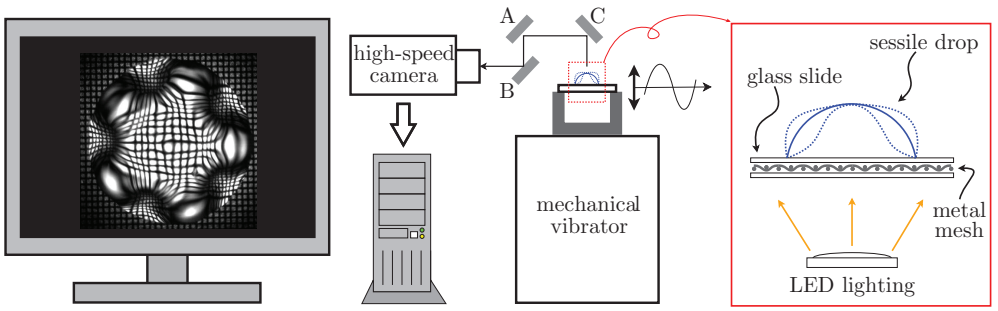

FIG. 2. (Color online) Schematic of imaging platform. Shown in the red (rightmost) box are the key components: mesh pattern and LED light source under the drop. Light rays from LEDs are refracted by the drop's deforming surface, reflected into the high-speed camera by mirrors A, B, and C, and convey a deformed mesh pattern to the computer, thereby visualizing the deformation of the drop's surface. A signal generator (not shown) oscillates the surface sinusoidally in the direction perpendicular to the plane of the surface.

surfaces that are designed to achieve a specific contact angle range (60°–70°). Glass surfaces were treated with 3-aminopropyltriethoxysilane (APTES) to achieve contact angles in this range. Wettability of coated glass slides was characterized by measuring the contact angles of 20 μL drops on the surfaces. Contact angles were measured using static images of drops before using the same drop in oscillation experiments. Details of surface preparation, functionalization, and characterization are provided in the Materials and Methods section.

Beneath the clear glass surface, a metal mesh with 50-μm weave is affixed. This metal mesh is the key ingredient that allows the deformation patterns to be identified from the top view. To affix the metal mesh beneath the functionalized surface securely, a second glass slide is used to create a sandwich structure with the 2×2 cm^2 metal mesh between the slides. White light emitted by light-emitting diodes (LED) from below the drop passes through woven metal mesh and is refracted by the drop's surface. As the drop deforms, the mesh pattern is distorted, allowing clear visualization of the unique patterns of troughs and peaks on the drop surface. Refracted light is reflected by mirrors C, A, and B and finally transmitted to a high-speed camera (Fig. 2). By rotating the mirrors together by 90°, side views of a drop can also be obtained. This technique works better for drops for which light is refracted through only one liquid-gas interface. That is, it is better for sub- than superhemispherical drops.

In experiments, each sessile drop is excited by a sinusoidal signal of a prescribed frequency. The range of frequency is 30–1100 Hz. minimal driving amplitude is applied to induce the resonance modes: For zonal modes, peak accelerations range from $0.1g$ to $1g$; while sectoral and tesseral modes require higher ($>1g$) accelerations. The highest acceleration among all experiments was $100g$. The sessile drop itself consists of pure water of 20 μL volume. With respect to these experimental parameters, Reynolds (Re) and Bond (Bo) numbers are defined as

$$\mathrm{Re} \equiv \frac{ar}{\omega\nu}, \quad \mathrm{Bo} \equiv \frac{\rho g r^2}{\sigma},$$

where a is the driving acceleration, r is the footprint radius of drop (typically around 2.5 mm), ω is the driving frequency in radians per second, ν is the kinematic viscosity of water, ρ is the liquid density, g is the gravitational acceleration, and σ is the surface tension. For all experiments, Re is approximately 200, while Bo is less than 0.5, hence the influence of viscosity is insignificant and surface tension dominates gravity.

B. Identifying observed shapes

As described in the Introduction, we shall catalog observed shapes according to the zonal, sectoral, and tesseral classification of spherical harmonics using the indices (k,l). Examples of all three different types of modes are presented in Fig. 3. Video files for selected modes are also available in the Supplemental Material [38]. As can be seen from the snapshots in the bottom two rows in Fig. 3, distortion of the mesh pattern by zonal modes is axisymmetric to the eye. The (3,3) and (5,5) modes exhibit one single layer of azimuthal wave patterns with three and five peaks, respectively. For the tesseral modes, the (5,3) mode possesses a Y pattern inside a triangle and the (7,5) shows a star of five vertices in a pentagon. Notice that for all combinations of k and l, $k + l =$ even numbers, consistent with Lamb half-drops.

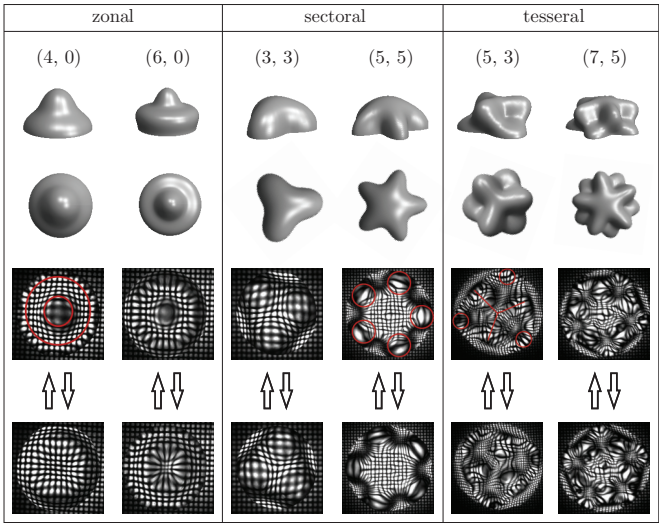

FIG. 3. (Color online) Examples of zonal, sectoral, and tesseral modes, where the numbers in the brackets are degree k and order l of the associated Legendre function specified in Eq. (2), according to which the 3D surfaces are rendered in rows 1 and 2. Images in rows 3 and 4 are top-view snapshots from experiments. The two snapshots for each mode differ temporally by one half-period of oscillation.

To further illustrate the scheme of mode identification, the image in column 1, row 3 of Fig. 3 is marked with red circles. These marks indicate the location of the nodal circles of the surface wave. According to the axisymmetric distortion of the underlying mesh pattern, the corresponding mode is zonal and possesses no azimuthal wave pattern, and hence a zero azimuthal wave number: $l = 0$. In addition, because the two nodal circles intersect any diameter of the drop four times, or alternatively the surface disturbance exhibits four zero crossings, $k - l = 4$, we find $k = 4$. Therefore the zonal mode is identified as a (k,l) = (4,0) mode. This scheme facilitates the identification of any mode with an axisymmetric mesh deformation.

The sectoral and tesseral modes are identified based on their polygonal profiles from the top views. Two examples are provided in Fig. 3, columns 4 and 5. The similarity between the image marked with red circles in column 4, row 3, with the simulation, column 4, row 2, is apparent: Both exhibit a pattern of one single star pattern with five vertices, which suggests that the former indeed results from the refraction of light across a deformed drop interface of the same qualitative geometry as the latter.

Similarly, in Fig. 3, column 5, the observed image is associated with the simulated image of a (5,3) mode by recognizing the marked "Y" pattern inside the outer triangle. Notice the primary difference between experimental images and simulations: Drops in experiments exhibit an approximately circular footprint, while drops in simulations exhibit a noncircular footprint. This difference is clarified by the fact that experimental drops are observed to possess limited mobility of their contact lines, while the simulations

assume completely mobile contact lines, as consistent with assumptions leading to Lamb half-drops.

C. Estimation of observed resonance frequencies

For all observed modes, the observed resonance frequencies f_o are estimated from image sequences as

$$f_o \approx f_s \frac{N_c}{N}, \tag{3}$$

where f_s is the sampling frequency or frame rate for recording the image sequence and N is the number of frames within which the drop completes N_c cycles of oscillation. A detailed description of the method and an error analysis is provided in the Appendix. With the current experimental setups, errors of measured frequencies are less than 3%.

D. Harmonic vs subharmonic resonance: Zonal and nonzonal modes

All observed zonal modes oscillate harmonically with respect to the driving signal. As shown in Fig. 4, the driving frequencies (f_d) are plotted against observed resonance frequencies (f_o) for the following modes: zonal modes with $k \leqslant 14$, sectoral modes with $k \leqslant 10$, and tesseral modes with $k \leqslant 10$, $k = l + 2$. With virtually undetectable deviation, the driving and observed frequencies are equal for all zonal modes. In contrast, sectoral and tesseral modes do not oscillate with the same frequency as the driving signal. Instead, these nonzonal modes exhibit $f_d \approx 2 f_o$ and therefore are half-frequency, subharmonic modes. Additional frequency comparisons for harmonic vs subharmonic modes are in the Appendix.

A qualitative explanation for such distinction between harmonic and subharmonic responses is that since the driving signal is vertical oscillation, it is axisymmetric with respect to the base state of a sessile drop. Prior to breaking the axisymmetry, zonal modes emerge. To synchronize with the driving signal, these modes must oscillate at frequencies close to that of the driving signal. At sufficiently high driving amplitudes, the axisymmetry breaks down and sectoral and/or tesseral modes emerge. These possess two azimuthally

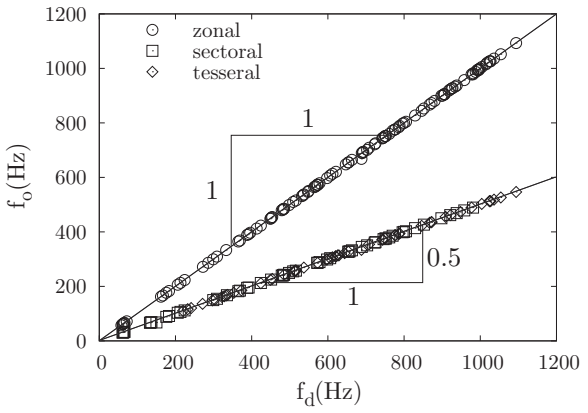

FIG. 4. Demonstration of distinction between harmonic and subharmonic modes: Zonal modes exhibit $f_d \approx f_o$ and therefore are harmonic modes. In contrast, the sectoral and tesseral modes exhibit $f_o \approx 0.5 f_d$ and are subharmonic modes.

conjugate states of maximal deflection, such as those shown in rows 3 and 4 of Fig. 3. To achieve equal temporal presence while synchronizing with the driving signal, either state of deflection spans one complete oscillation cycle of the driving signal. Therefore it takes the nonzonal modes two cycles of excitation to complete one cycle of oscillation, and hence they exhibit a half-frequency or subharmonic response. In contrast, since zonal modes possess no azimuthal deflection, resonance of zonal modes requires only synchronizing one state of deflection with the driving signal, a harmonic response.

Interestingly, the two types of resonance behaviors have been observed to coexist simultaneously within the same drop driven by the same signal. Our observations of these cases reinforce that a zonal mode oscillates twice as fast as any nonzonal mode that mixes with it. We will describe the mode-mixing phenomena in detail later.

E. Catalog of observed shapes

With reference to Eq. (2) and among the modes with $k \leqslant 10$ and $l \leqslant 10$ (corresponding to the first 35 modes), all but the $(k,l) = (10,4)$ are observed and recorded. In addition, two zonal modes are repeatedly observed mixing with higher-order sectoral and tesseral modes: the (12,0) and the (14,0). Indices (k,l) are useful as they establish the relationship to Lamb half-drops. However, k is not the polar wave number observed. Nevertheless, there is a simple relationship to the polar wave number where

$$n \equiv \frac{k-l}{2} + 1. \tag{4}$$

Notice that, by this definition, n represents the number of layers of wave peaks for any given mode. For zonal modes, $l = 0$, which possess no azimuthal variations, n is the number of layers of polar wave peaks or troughs observable from the side views. Sectoral modes are those that have $l > 0$ and $n = 1$, which observationally means the modes with one single layer of azimuthal variation. All others (those with $l > 0$ and $n > 1$) are tesseral modes. Top-view snapshots of all observed modes are cataloged in Fig. 5. We are unsure why the mode $(n,l) = (4,4)$ has not yet been observed. It is likely to be discovered with future experimental probing.

III. COMPARISON OF EXPERIMENTAL OBSERVATIONS AGAINST THEORY

A. Lamb half-drops against observed zonal mode

For all modes, the resonance frequencies are estimated according to Eq. (3) and compared to predictions of Eq. (5):

$$f_t(k,m) = \sqrt{\frac{\sigma}{3\pi \times 2m} k(k-1)(k+2)}, \tag{5}$$

where σ is the surface tension, k is the polar wave index, and $m = 20$ mg is the mass of each sessile drop (20 μL in volume) in experiments. The Rayleigh and Lamb theory describes free oscillation of spherical drops in space, while in experiments the drops are sessile and mechanically vibrated. Nonetheless,

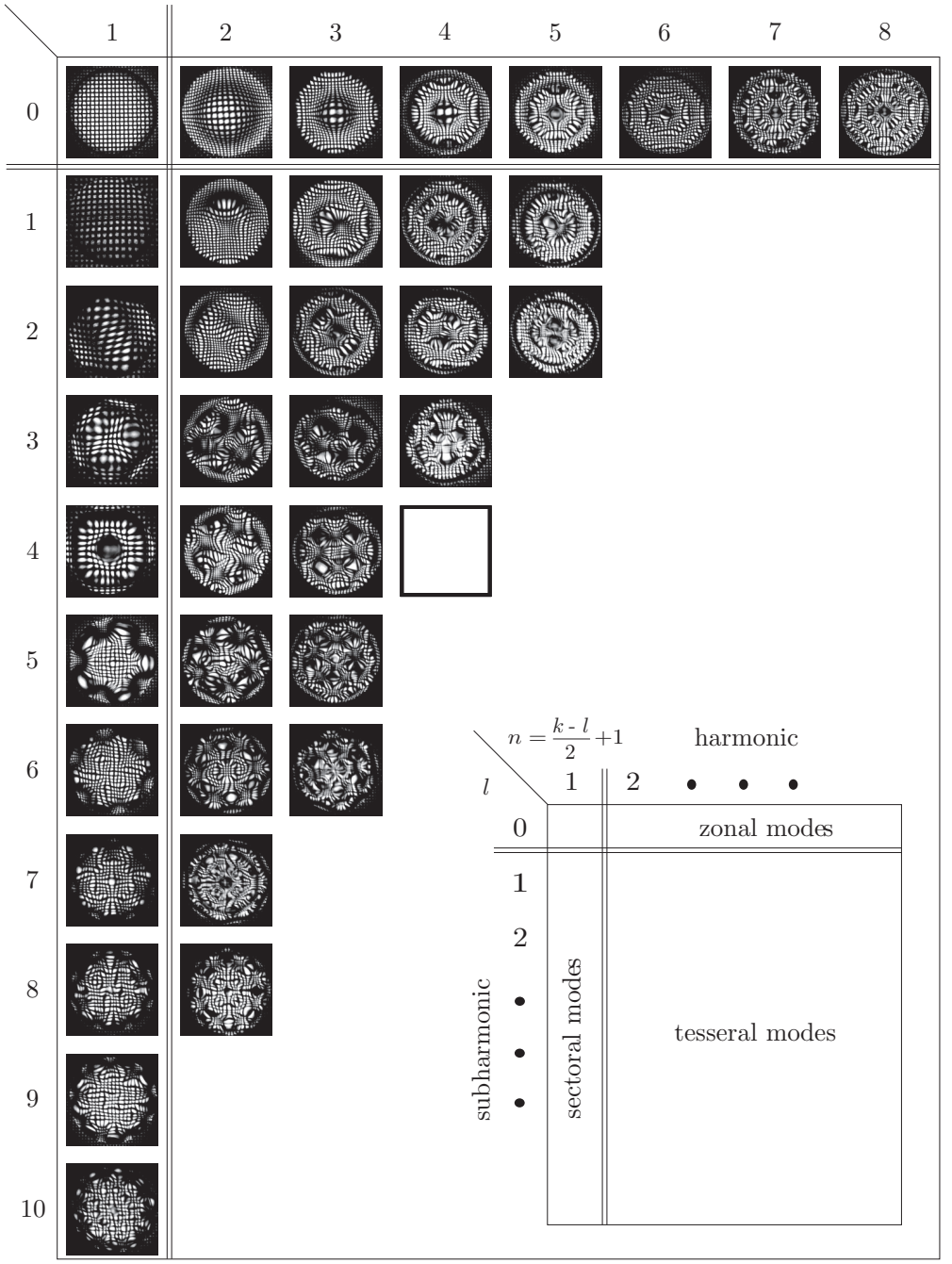

FIG. 5. Summary of mode shapes observed in experiments. For reference, the picture for $(n,l) = (1,0)$ is the top view of a static drop. Modes are arranged by physical appearance and nature frequency responses (i.e., subharmonic and harmonic): As partitioned by the double vertical line, zonal modes ($l = 0$) are axisymmetric and harmonic modes; others are subharmonic modes lacking axisymmetry. Sectoral modes only differ from tesseral modes by having $n = 1$.

it is of interest to determine how well the classical theory can capture the observed resonance frequencies of sessile drops.

To compare the sessile drop equivalent to the Rayleigh and Lamb half-drop, ideally, the sessile drop should be perfectly hemispherical (90° contact angle) with freely moving contact lines (no pinning). The experiments would then correspond most closely to the theory and the estimated resonance frequencies of sessile drops with mass m could be compared to eigenfrequencies of spherical drops with mass $2m$. Notice here we restrict to undisturbed drops that are subhemispherical. A subtle point is then how to account for the mass m to fairly compare to the Lamb prediction.

One way to address this point is to remove the capillary time scale $(3\pi \times 2m \div \sigma)^{1/2}$ in Eq. (5) by normalizing frequencies. For experimental data, the average frequency $\bar{f}$ of (2,0) mode in all observations is calculated first. The ratio q of the observed resonance frequency f_o to $\bar{f}$ is subsequently computed. For theoretical predictions, the same ratios q are calculated by normalizing all predicted eigenfrequencies by that of the (2,0). These frequency ratios q are plotted together in Fig. 6.

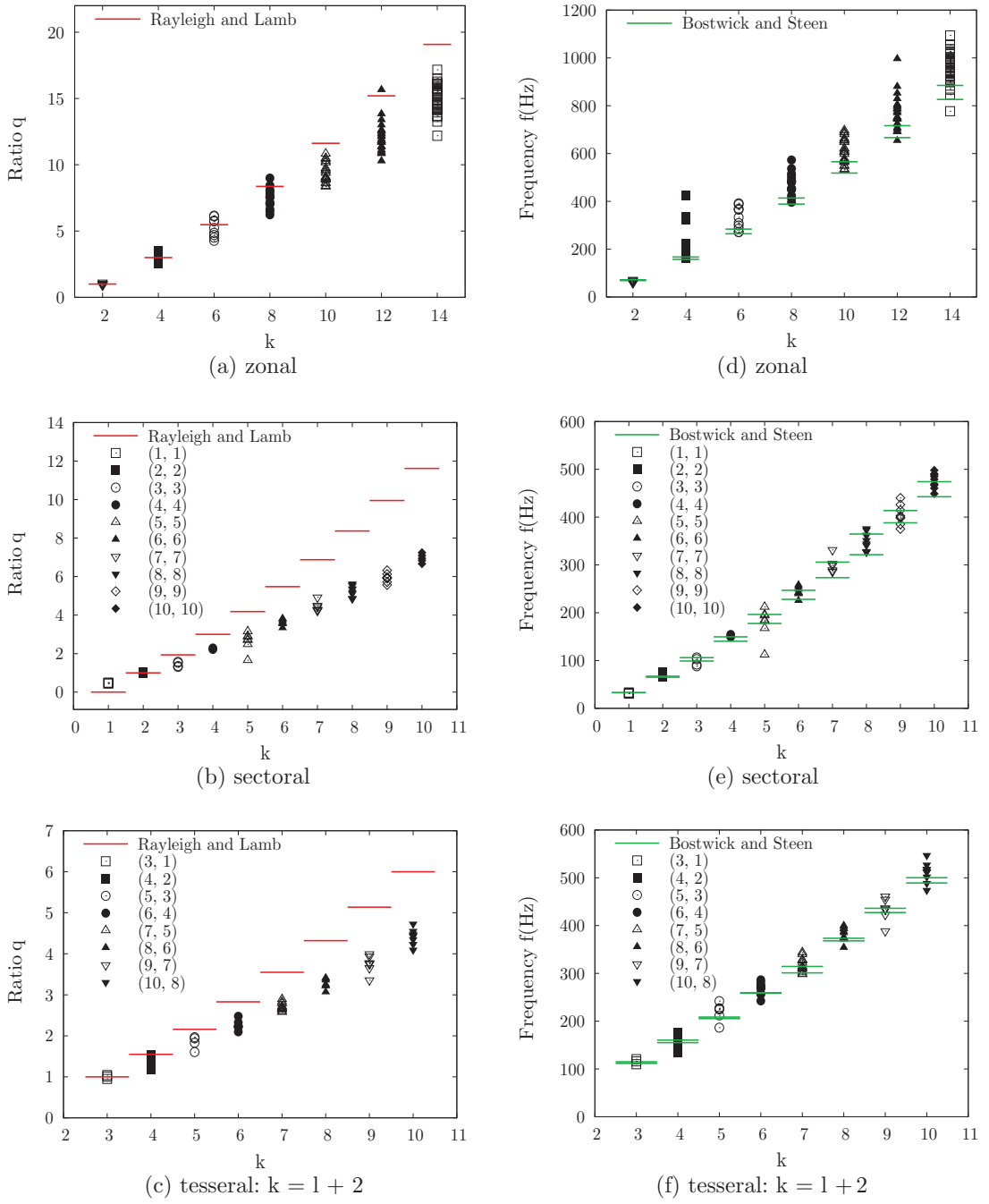

FIG. 6. (Color online) Comparison of normalized resonance frequencies and frequency scaling prediction by Rayleigh and Lamb [1] [(a)–(c)] and Bostwick and Steen [(d)–(f)]: (a), (d) zonal modes; (b), (e) sectoral modes; and (c), (f) tesseral modes with $k = l + 2$.

Comparisons of actual frequencies are found in the Appendix. As is observable from the figure, for $k \leqslant 10$, the normalized eigenfrequencies, or ratio q, lie above the data points. Because of the normalization, the capillary time scale, or in fact the choice of volume, density, and surface tension, no longer affects the result, and it is only the predicted scaling that is compared to the scaling trend of experiments. According to Fig. 6(a), there is an apparent mismatch of the theory and experiment for zonal modes.

Recall the second fundamental distinction between theory and experiments: The Lamb half-drops correspond to a sessile drop with completely free contact lines. However, in reality, these drops exhibit nearly fully pinned contact lines. The anticipated impact of this condition is to spread the experimentally observed frequencies for each mode as well as to lower the mean frequency.

B. Lamb half-drops against observed sectoral and tesseral modes

In this section, we compare the experimental frequency measurements of sectoral and tesseral drops with Eq. (1). To make the comparison, independent of the specified capillary time scale in Eq. (5), the same normalization procedure for

zonals is used. For sectorals, the experimental and predicted eigenfrequencies are normalized by the average of the frequencies of the observed (2,2) mode and by the Lamb (2,2) frequency, respectively. Note that the (2,2) eigenfrequency is the first nonzero Lamb frequency. For tesseral modes, the frequencies are all normalized by those of the $l = 1$ modes, i.e., (3,1), (5,1), (7,1), and (9,1), respectively. The results are presented in Fig. 6(b) for sectoral modes and Fig. 6(c) for tesseral modes with $k = l + 2$. For other tesseral modes, see the Appendix. The Rayleigh and Lamb theory overshoots the experimental data. We conclude that the Rayleigh and Lamb theory is insufficient for describing behaviors of these modes.

C. Bostwick and Steen sessile drop

We now compare the experimental data with predictions from the Bostwick and Steen solution of sessile drop oscillations. The Bostwick and Steen model considers the free oscillation of an inviscid sessile drop with prescribed contact angle and contact-line mobility. The spherical-cap base states are parametrized by the scaled volume or, alternatively, the equilibrium contact angle. In either case, there is a one-parameter family of base states. The contact-line constitutive behavior is characterized by a mobility parameter with two limiting cases: the fully mobile contact line and the pinned contact line. For purposes of this paper, consistent with experimental observation, we only consider pinned contact lines. The governing equations are analogous to the Rayleigh and Lamb free drop equations with the addition of the pinning boundary condition and the no penetration velocity condition on the substrate plane. The central challenge to solving these equations comes with obtaining Laplace equation solutions for the velocity potential on a spherical-cap domain with variable boundary data. Through a functional analytic approach, much like that used for the drop with the constraint of a latitudinal belt [23], the equations have been solved for eigenmodes and eigenfrequencies. Details are presented elsewhere. The final step involves a numerical computation. Consequently, a closed form expression like Eq. (1) is not available, but the results are obtained via a look-up table. This look-up table for pinned sessile drops is provided in the Supplemental Material [38] along with instructions on how to use it. In summary, the Bostwick and Steen modes take the form

$$r(\theta,\psi) = 1 + \varepsilon f(\theta)\cos(l\psi), \qquad 0 \leqslant \theta \leqslant \alpha, \quad 0 \leqslant \psi \leqslant 2\pi, \tag{6}$$

where $f(\theta)$ and frequencies are determined computationally. The profile $f(\theta)$ is associated with an index k. The frequencies reported below, as they depend on wave numbers and contact angle, come from the look-up table.

For each mode with wave indices (k,l), based on the experimental parameters of liquid volume (20 μL), surface tension (72×10^{-3} N/m), density (1000 kg/m^3), and pinned contact lines, two eigenfrequencies are calculated, each corresponding to the maximal and minimal contact angles observed for those sessile drops, respectively. These bounds, based on the observed contact angle spread, are represented by the solid lines (green, online) in Figs. 6(d)–6(f). The result is presented in Fig. 6(d) for all observed zonal modes. In contrast to the trend of uniform overestimation by the Rayleigh and Lamb drop prediction, the Bostwick and Steen prediction exhibits a reasonable agreement with the experimental result, as the predicted frequencies fall within the lower portion of the experimental data. Because of the neglect of viscous effects, bandwidths of predicted eigenfrequencies are small and prediction cannot be expected to capture a wide spread of frequencies.

D. Bostwick and Steen drops against observed sectoral and tesseral modes

A similar comparison between experimental data and the Bostwick and Steen prediction for sectoral modes is presented in Fig. 6(e). Reasonable agreement is noted. Results of the same comparison for tesseral modes with $k = l + 2$ are shown in Fig. 6(f). Comparisons for other tesseral modes are shown in the Appendix. Among the observed modes, the ones with fewer layers of azimuthal variations exhibit a better match between experiment and prediction. But even for the higher modes, the theoretical predictions fall within the spreading of experiment data, therefore suggesting a credible consistency between the experiments and the Bostwick and Steen predictions.

IV. MODE MIXING

In experiments, simultaneous coexistence of different modes is frequently observed. Mixed modes are typical, especially for modes with more complex shapes. To illustrate the phenomena, an example image sequence of a relatively pure (5,3) mode is first presented in Fig. 7 to facilitate subsequent comparison. In Fig. 7, at $t = 1.75$ ms and $t = 4.47$ ms the drop apparently exhibits a Y pattern inside a triangle, which confirms the similarity of the observed pattern with the postulated (5,3) mode in Fig. 3.

In contrast to the relatively pure case shown in Fig. 7, an image sequence exhibiting the mixture of a (5,3) mode with an (8,0) mode is shown in Fig. 8. At $t = 0$, 1.6, 2.0, and 3.8 ms, a rounded triangular wave pattern close to the contact line of the drop is first identified. The image for $t = 1.6$ and 3.8 ms exhibit Y patterns inside their outer triangular azimuthal wave patterns. Consider the common feature of possessing Y patterns inside an outer triangle for the two frames and those for $t = 1.75$ and 4.47 ms in Fig. 7. Apparently the image sequence in Fig. 8 contains (5,3) as one of its wave components. In contrast, by visually examining images for $t = 0.8$ and 2.8 ms, one observes roughly identical axisymmetric distribution of mesh pattern deformation, which indeed suggests the coexistence a zonal mode with the tesseral, (5,3) mode. With careful inspection of images for $t = 0.8$ and 2.8 ms, one finds that the zonal mode is (8,0). Indeed, such coexistence also explains why the images for $t = 0$ and 2.0 ms show a smaller rounded inner pattern instead of a sharper triangular or Y pattern. Furthermore, one finds within approximately 3.8 ms, the (5,3) mode completes one single period of oscillation, while two roughly identical axisymmetric profiles ($t = 0.8$ ms and $t = 2.8$ ms) appear approximately every 2 ms. Notice that the driving frequency is 454 Hz. By examining the original image sequence from which images in Fig. 8 are extracted, one finds that $N = 198$ and $N_c = 9$, both of which are associated with the occurrence

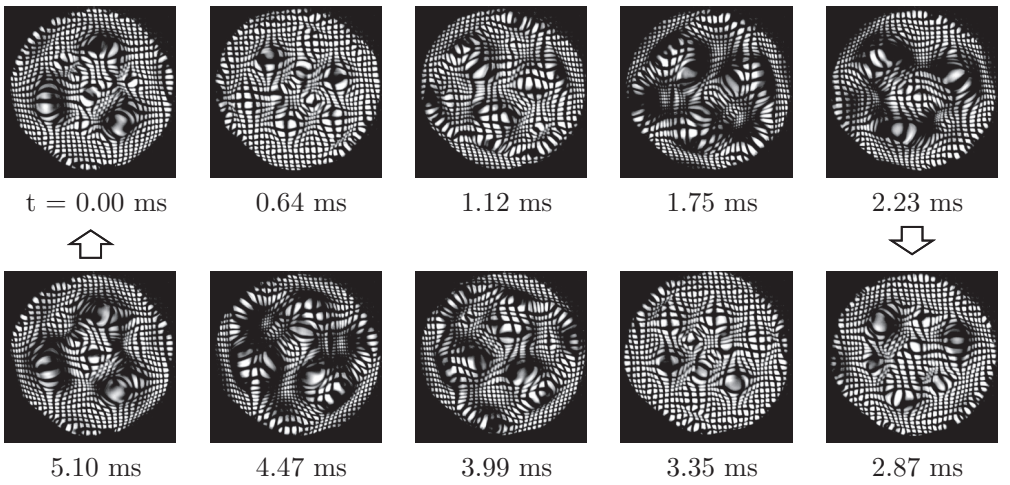

FIG. 7. Image sequence of a relatively pure (5,3) mode. The image of $t = 1.75$ ms corresponds to that with $(n,l) = (2,3)$ in Fig. 5.

of the lower-frequency, (5,3) mode. Therefore the observed resonance frequency is 227.27 Hz, according to Eq. (2). Since (8,0) repeats twice when (5,3) completes one cycle, the (8,0) frequency is 454.54 Hz. Therefore the image sequence in Fig. 8 shows that a single droplet, which is oscillated by a sinusoidal signal of one single frequency, simultaneously exhibits two distinct modal behaviors: one being a harmonically generated zonal mode, and the other a subharmonically generated tesseral mode. To further illustrate the ubiquity of mode mixing, two other examples are described in detail in the Appendix.

In this section, the observed mode-mixing phenomena is compared to theoretical prediction for either Rayleigh and Lamb or Bostwick and Steen. We denote the observed frequencies of harmonic and subharmonic modes as f_{oh} and f_{os}, and the theoretically predicted frequencies for the former and the latter as f_{th} and f_{ts}, respectively. In order for a subharmonic mode to mix with a harmonic mode, because the observed subharmonic modes all belong to the half-frequency type (i.e., $f_{os} \approx f_d \div 2$), $2 \times f_{os}$ must be close to f_{oh} so that both modes can simultaneously synchronize with the same driving signal of frequency, f_d. Based on this physical argument, we compare the theoretical frequency predictions to the observed frequencies for a pair of harmonic and subharmonic modes which are observed to mix. To facilitate comparison, a frequency ratio c is defined as

$$c \equiv \frac{2 f_{ts}}{f_{th}}.$$

We denote the ratios based on Rayleigh & Lamb and Bostwick & Steen theories as c_{RL} and c_{BS}. If $c = 1$ exactly, this means that the theory predicts mode mixing perfectly. Therefore, a deviation of c from 1 predicts a measure of how well a theory predicts mode mixing. Based on the Rayleigh and Lamb theory, the ratio for the (5,3) and (8,0) modes equals exactly 1, precisely matching the experimental results. For the Bostwick and Steen theory, consider that the static contact angle for this experiment was 67°. Using the look-up table (Supplemental Material), the frequency ratio is 1.02. Since both ratios deviate from 1 by less than 3% (which is the error in the frequency estimation in experiments), both theories

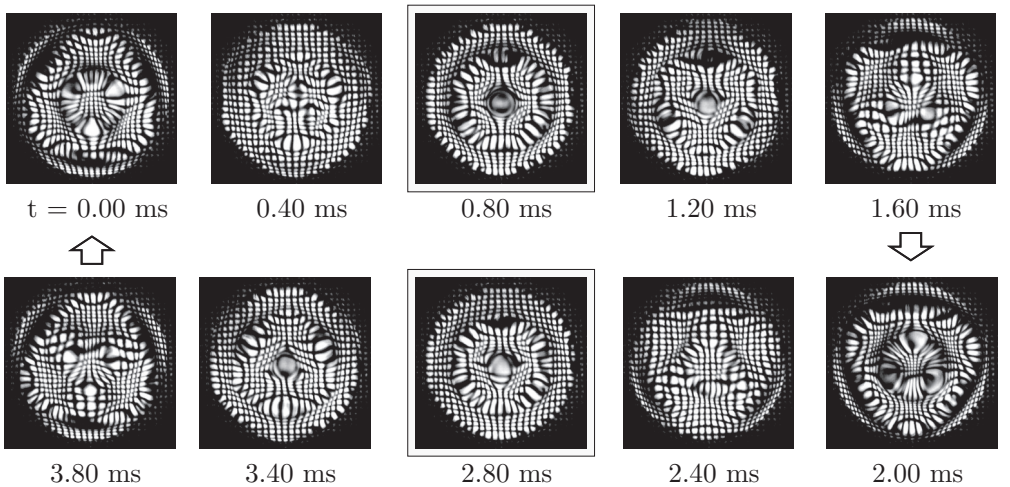

FIG. 8. Image sequence of a $(k,l) = (5,3)$ mode mixing with a $(k,l) = (8,0)$ mode. The (8,0) appears twice in one period of the (5,3) and oscillates with the same frequency as the driving signal. The (8,0) is boxed to highlight that mode. The shape is confirmed by comparing the boxed images to that of $(n,l) = (5,0)$ in Fig. 5.

TABLE I. Frequency ratios of mixing modes based on the Rayleigh & Lamb and Bostwick & Steen theories.

Mixing pair	c_{RL}	c_{BS}
(5,3) + (8,0)	1.000	1.020
(7,7) + (10,0)	1.183	1.037
(8,6) + (12,0)	1.100	1.044

predict that mode mixing will occur for this example with similar accuracy. Extending this analysis for the two other examples shown in the Appendix, frequency ratios for the mixing modes are tabulated in Table I. From these results we observe the Bostwick and Steen theory predicts frequency ratios to within $1+/-5\%$, while the predictions based on the Rayleigh and Lamb theory deviate significantly for the last two cases (by $\sim$18% and 10%, respectively).

V. DISCUSSION

In our experiments to good approximation, undisturbed drops have a spherical-cap shape with contact angles ranging from 60° to 80° and with pinned contact lines, to the extent that no depinning is detectable, at least for the accelerations and amplitudes reported in this study. As manifest in the catalog of observed modes, Fig. 5, this deviation from Lamb half-drops is sufficient to fully break the degeneracy of the Lamb spectrum. That is, the first 29 nonzonal modes have been observed. Enumeration of modes in the catalog is based solely on arguments of symmetry breaking of the degenerate Lamb spectrum. This is to be expected since, as surface vibrational modes, these disturbed nonhemispherical sessile drops must be periodic in the azimuthal direction having a meridional wave structure, hence retaining the relevance of the (k,l) labeling. In summary, the (k,l) labeling is useful for relating modes back to the Rayleigh and Lamb spectra. However, for purposes of identifying the modes from experimental images, a better scheme is to use the wave numbers in the meridional and azimuthal directions $[n = (k-l)/2+1, l]$. The wave number n has the convenient interpretation as the number of vertical layers for any mode. Zonals with up to eight and tesserals with up to five vertical layers have been documented (Fig. 5). In fact, up to the technical limits of our experiments, all predicted modes have been observed, except for the $(n,l) = (4,4)$ mode or $(k,l) = (10,4)$ which falls at the boundary of the observation limits (empty box in Fig. 5). In view of some confusion in the literature regarding mode labels [16], it is of clear benefit to have a standard way for referring to a particular mode. Such a standard should be based on observation as closely as possible.

The frequencies of the various modal structures are also expected to reflect the symmetry breaking. Indeed, measured frequencies $f_o(k,l)$ show that the common frequencies (eigenvalues) of the Lamb half-drops, same k, any l, have split into separate frequencies (eigenvalues) for each different (k, l) mode (eigenfunction). We first compare directly to the degenerate Rayleigh and Lamb spectrum. More precisely, Figs. 6(a)–6(c) compare frequency gaps of the measured against Lamb. Although the zonal comparison [Fig. 6(a)] is ambiguous, the sectoral and tesseral modal comparisons [Figs. 6(b) and 6(c)] show more clearly that the Lamb spectrum overpredicts, especially for a higher modal index k. We should note that the most challenging aspect of the experiments is controlling the equilibrium contact angle. Despite careful and consistent surface preparation, surface aging and/or inhomogeneity often are seen. For a single drop and a single experiment, the contact angle has been observed to vary by as much as 10° from beginning to end (5 min duration). From experiment to experiment (same batch, different drop) and from beginning to end (same experiment), the contact angle could vary by as much as 20°. On the plus side, contact angles were monitored to within 5°. That is, variation could not be precisely controlled but could be precisely monitored. This explains the contrast of the spread in frequencies reported in Fig. 6 to the precision of those in Fig. 4. Different contact angles are expected to have different frequencies [16,33]. To further confirm the frequency splitting illustrated in Figs. 6(a)–6(c), we compare to predictions for drop vibrations of the solution of the eigenvalue problem that takes account of contact angle (and pinning) [Figs. 6(d)–6(f)]. In Figs. 6(d)–6(f), for each mode, the minimum and maximum predicted frequency corresponding to the monitored minimum and maximum contact angle, are plotted alongside the measurements. The spread in measurement typically exceeds the band in prediction, certainly owing to deficiencies of the model and imprecision in the experiment. A more detailed discussion is beyond the scope of this paper.

In contrast to the zonal modes, sectoral and tesseral modes respond subharmonically, consistent with the literature where nonaxisymmetric response has been long associated with parametric excitation, the Faraday problem being the canonical example from fluid physics. According to Fig. 3, nonzonal oscillations can be thought of as built from two conjugate states, each with a phase shift of azimuthal angle equal to one-half the symmetry angle. For example, for the (3,3) mode, the symmetry angle is $\pi/3$ and the phase shift is $\pi/6$. The subharmonic response can be thought of as an average between the two states, neither being preferred, and hence it takes twice the period to sample equally. The driving frequency must, accordingly, be half the fundamental frequency. Note that the measured nonzonal frequencies compare well to those predicted by Bostwick and Steen from symmetry-broken solutions, Figs. 6(e) and 6(f).

To what extent does nonlinearity from contact-line hysteresis or otherwise play a role in the transitions to nonzonals (or, for that matter, to zonals)? We do not address the question in this paper. Our main point is the utility of the Lamb half-drop spectrum for classifying observed modes and of the Bostwick and Steen spectrum for the splitting of frequencies. To the extent that, in the absence of any contact with a solid, sectoral oscillations of a free drop are also subharmonic [18] supports our contention that contact line and any nonlinear effects are not essential to the parametric mechanism. Nonlinear effects in drop dynamics are discussed in a general way in Ludu [39], for example.

Finally, the observed mode mixing (Figs. 8, 14, and 15) is almost certainly a result of nonlinearity. However, again, we place any discussion of this outside the scope of this paper. Our main point is that, for mode mixing to occur, the necessary relationship between frequencies can be predicted by the linear spectra. As shown for the example in Fig. 8,

$f_d = f_o(8,0) = 2 \times f_o(5,3)$. For any driving frequency, one can scan the spectrum and identify potentially mixing modes. There is a reasonable correspondence between linear theory predictions and observed mixing.

VI. CONCLUSIONS

There is a long history of applying or adapting the Rayleigh free drop spectra [Eq. (1)] to observations of vibrations of liquid interfaces, no matter how the interface is constrained, if at all. We argue that the zonal, sectoral, and tesseral labeling associated with these mode shapes remains valid since they capture the separation of variables that will apply for any azimuthally periodic shape arising from the spherical harmonic solution of the underlying Laplace's equation. In this sense, the resilience of the Rayleigh and Lamb spectrum can be explained.

On the other hand, these classic spectra are degenerate in that the doubly infinite set of frequencies $f(k,l)$, where $k = 1, 2, 3, \ldots$ and $l = 0, 1, 2, \ldots$, collapse into $f(k)$. Sufficient symmetry breaking will break this degeneracy and split the frequencies. The experiments reported demonstrate that a deviation from the hemispherical shape of only 10° or so is sufficient to yield measurable frequency splitting, especially for the higher k. Comparison against the Rayleigh and Lamb and Bostwick and Steen frequencies provide a quantitative metric of how much the Rayleigh spectrum is modified.

We have observed, identified, and cataloged the behavior of 36 of the first 37 resonance modes of sessile drops. We classify these modes as zonal, sectoral, or tesseral. According to our observation, zonal modes respond harmonically, while sectoral and tesseral modes respond subharmonically. Despite their fundamental distinctions, several examples show that the modes can mix without changing their respective individual mode dynamics as exhibited in the absence of mixing.

VII. MATERIALS AND METHODS

A. Materials

APTES 99+% was purchased from Gelest (Morrisville, PA). Glass slides (VWR VistaVision, catalog No. 16004-430, $3'' \times 1'' \times 1$ mm) were purchased from VWR International (Radnor, PA). Stainless steel woven metal mesh (#150, part number 85385T875) was purchased from McMaster (Santa Fe Springs, CA). Ethanol (reagent alcohol, absolute, CAS# 64-17-5; Macron Chemicals) and acetone (CAS# 67-64-1; Macron Chemicals) were purchased from VWR International (Radnor, PA). High-purity compressed nitrogen was purchased from Airgas (Salem, NH). Sulfuric acid (95–98% min., MW 98.08, CAS# 7664-93-9) was purchased from VWR International (Radnor, PA). Hydrogen peroxide solution (50 wt%, 516813-500ML, CAS# 7722-84-1 MW 34.01 g/mol) was purchased from Sigma-Aldrich (St. Louis, MO).

B. Preparation of surfaces

Glass slides were prepared by first sonicating them for 20 min in water to remove any solid particles on their surfaces. To remove any organic contaminants, the slides were then soaked for 20 min in piranha solution (70% sulfuric acid/30% hydrogen peroxide). Afterwards the glass slides were rinsed by de-ionized (DI) water (purified by an Elga Ultra SC MK2, Siemens) for at least 10 min and kept fully immersed under DI water until the next step. The interior surface of a 400-ml staining dish and a glass rack were rinsed, in order, with (1) soap, (2) RO water, (3) ethanol, and (4) acetone. The dish and rack were then blown dry by nitrogen gas and baked in the oven for 15 min. 200 ml of acetone and 8 ml of APTES silane were deposited in the cleaned staining dish. Each glass slide was dried by blowing high-purity nitrogen gas and placed onto the immersed glass rack in the APTES silane solution for 20 min. After the 20-min soaking, the samples were moved to an oven for heating at 85 °C for 20 min to secure the bonded APTES molecules on the glass surface.

Prior to the first use in experiments, all coated glass slides were rinsed with ethanol and DI water and dried with high-purity nitrogen gas. For each coated glass slide, another uncoated slide is cleaned by sonicating for 20 min. The two slides were then tightly taped together to sandwich a piece of woven metal mesh of approximately 2×2 cm^2 between them.

C. Characterization of surfaces

Wettability of coated glass slides was characterized by measuring the contact angles of 20 μL drops on the surfaces. Contact angles were measured using static images of drops before using the same drop in oscillation experiments. Images were processed using ImageJ 1.45. Based on 222 sets of contact angle measurements for four batches of 40 glass slides in total, the average contact angle was approximately 68.6°, with a standard deviation of 5°.

ACKNOWLEDGMENTS

The authors acknowledge Dr. Michel Y. Louge for his generous supply of the VTS-100 mechanical oscillator used in this work. The authors appreciate the helpful discussions and assistance in constructing the custom mechanical and electrical hardware used in this work from research specialist Glenn Swan, Dr. Bruce Land, and David Hartino. The authors acknowledge helpful and inspiring discussions with Dr. Michel Y. Louge, Dr. Alan T. Zehnder, Dr. Wolfgang H. Sachse, and colleague Donald Lee. Finally, the authors thank NASA (Grant No. NNX09AI83G), National Science Foundation (Grant No. CBET-1236582), and Xerox Corporation for financial support.

TABLE II. Optimal frame rate and the corresponding maximal spatial resolution.

Frame rate (fps)	5000	6270	7975	9100	10470
Resolution (pixel × pixel)	512 × 512	480 × 480	416 × 416	384 × 384	352 × 352

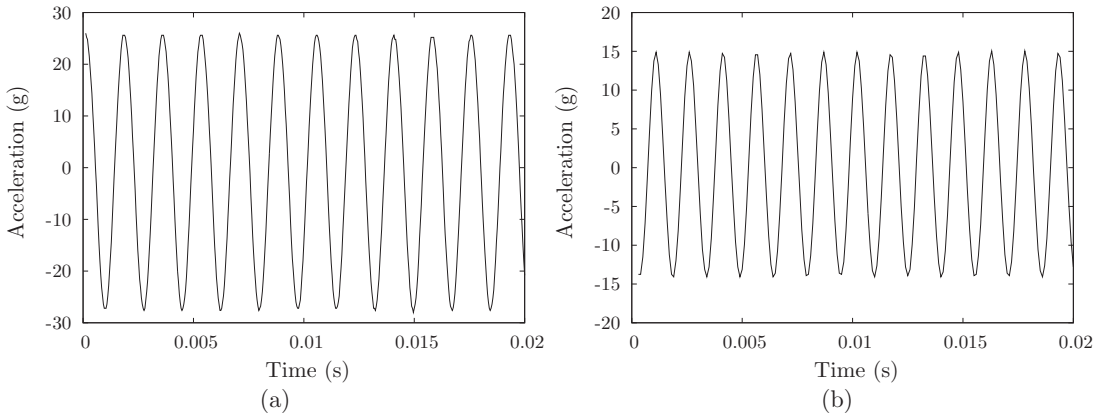

FIG. 9. Examples of measured accelerations. Driving and sampling frequencies, f_d and f_s, are (a) $f_d = 573$ Hz, $f_s = 25$ kHz; (b) $f_d = 658$ Hz, $f_s = 10$ kHz.

APPENDIX

1. Imaging resolution

In experiments, it is empirically found that a reasonable temporal resolution of image sequence is achieved if at least ten frames of images are recorded within one cycle of a zonal mode's oscillation. For nonzonal modes which lack axisymmetry, ten frames of images are needed for each half cycle of oscillation. Considering that zonal and nonzonal modes are harmonic and half-frequency subharmonic modes, respectively, frame rates (frames per second) for high-speed imaging are chosen to be at least ten times the driving frequency of the mechanical vibrator. Rather than simply recording images at ten times the driving frequency of mechanical oscillation, the frame rates are chosen among the set of optimal frequencies dictated by the HG-XL high-speed camera utilized in experiments. For this camera, the frame rates are partitioned and associated with a particular optimal spatial resolution as shown in Table II.

2. Characterization of the mechanical oscillation

To ensure the mechanical vibration is a purely monochromatic sine wave oscillating in the vertical direction, we have characterized the substrate motion by two methods. First, we made direct visual observation of the mechanical oscillation using high-speed image sequence. No lateral (i.e., nonvertical) oscillation was observed. Second, vertical accelerations were measured using an 8704B100 accelerometer (Kistler Instrument Corp., Amherst, NY) on the oscillation platform. The signal from the accelerometer was amplified first by a signal conditioner (model No. 5114, by Kistler Instrument Corp., Amherst, NY) and subsequently sent to and recorded by a digital oscilloscope (model GDS-1102-U, by GW Instek, Taiwan). Two examples of acceleration measurements are provided in Fig. 9. These examples illustrate that the sinusoidal driving signals are reasonably clean.

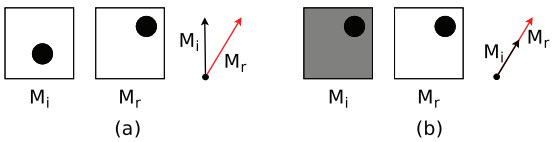

FIG. 10. (Color online) Comparison of $z[i]$ defined in Eq. (A1) and any inner-product-based norm: (a) both detect pattern translation, but (b) only $z[i]$ detect brightness variation.

3. Estimation of resonance frequencies

For all observed modes, the resonance frequencies f_o are estimated from image sequences from Eq. (3). Conceptually, any visually observable motion described by an image sequence must be conveyed by the variation of color or grayscale distribution from one image to another. For example, consecutive snapshots of an object moving with respect to a static background must exhibit some combination of translation, rotation, and deforming pattern of the object as its motion evolves, while given any static scene, if thousands of frames are recorded (especially if by high-speed imaging), little difference is expected between any two frames. In the current application where an image sequence describing periodic motions of an oscillating drop is concerned, with respect to a fixed reference image, evolution of the difference between the reference frame and any dynamic snapshot in the sequence is also expected to be periodic, provided an adequate norm quantifying the difference is adopted. To proceed, let the size of each frame be $a \times b$ pixels, and k and j

TABLE III. Error estimation of resonance frequencies.

N_c	$N_{\max}$	$N_{\min}$	N_r	$\varepsilon_{\max+}$ (%)	$\varepsilon_{\max-}$ (%)	$\varepsilon_{\min+}$ (%)	$\varepsilon_{\max-}$ (%)
1	200	101	99	0.002	0.003	0.010	0.010
2	200	68	64	0.005	0.005	0.043	0.044
3	200	51	47	0.007	0.008	0.113	0.118
4	200	41	36	0.010	0.010	0.232	0.244
5	200	34	30	0.012	0.013	0.420	0.446
6	200	29	26	0.015	0.015	0.690	0.739
7	200	26	18	0.017	0.018	0.997	1.077
8	200	23	16	0.020	0.020	1.449	1.581
9	200	21	11	0.022	0.023	1.948	2.143
10	200	19	10	0.025	0.025	2.632	2.924

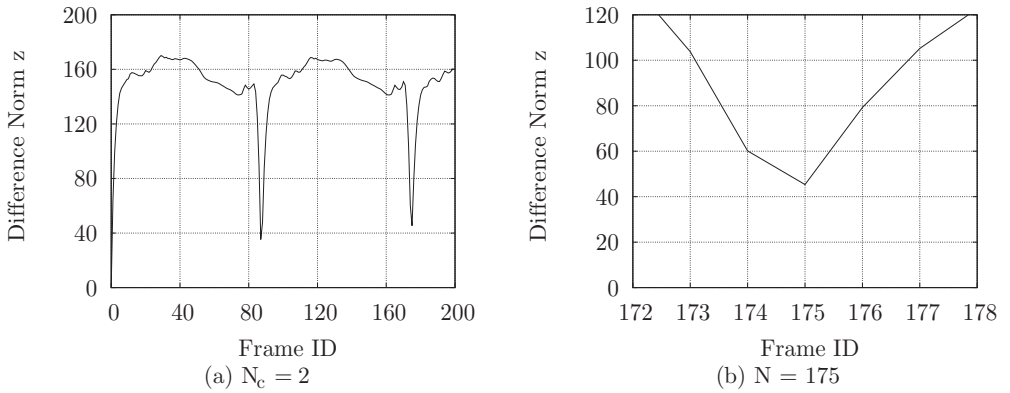

(a) $N_c = 2$ (b) $N = 175$

FIG. 11. An example of estimating N and N_c with Eq. (A2): (a) two notches in the plot gives $N = 2$; (b) the position of the second notch yields $N_c = 175$. Together with the 5000-Hz frame rate of the corresponding image sequence, the resonance frequency is $5000 \times 2/175 = 57.14$ Hz.

be the horizontal and vertical coordinates of pixels in images. Denote the matrix of the color or grayscale values of pixels in the reference frame and the i-th dynamic snapshot as $M_r[k, j]$ and $M_i[k, j]$, respectively. A norm $z[i]$ quantifying difference between the ith frame and the reference image is defined as

$$z[i] = \left\{ \sum_{j=0}^{a} \sum_{k=0}^{b} (M_i[k,j] - M_r[k,j])^2 \right\}^{1/2}. \quad \text{(A1)}$$

The choice of norm $z[i]$ in Eq. (A1) is based on its relatively broader coverage of difference between images. Formally, $z[i]$ quantifies the $\mathcal{L}-2$ norm of the difference between two images. Hence unless there exists absolutely no difference between any two corresponding pixels in two given images, a nonzero value of $z[i]$ will frankly indicate any slight variation of one image from the other. This provides a broader coverage of variation detection than, say, a norm based on inner product (i.e., just the difference in M_r and M_i's orientations), since with Eq. (A1), not only can any motion (e.g., translation, rotation, distortion, etc.) be detected and quantified, but also

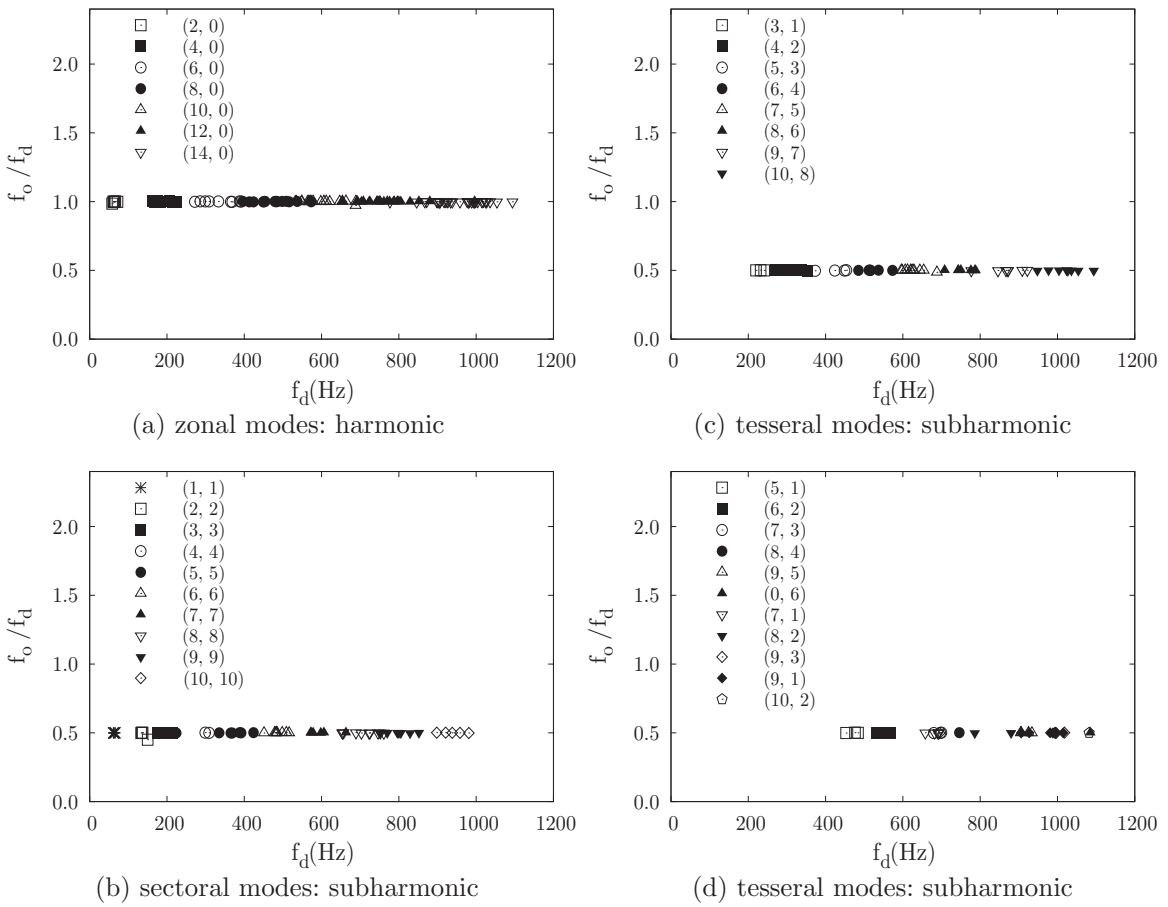

(a) zonal modes: harmonic (c) tesseral modes: subharmonic

(b) sectoral modes: subharmonic (d) tesseral modes: subharmonic

FIG. 12. Demonstration of harmonic and subharmonic modes: $f_o/f_d = 1$ (harmonic) for all zonal modes, and 0.5 (subharmonic) otherwise.

any flickering of lighting even if the scene remains perfectly static. As illustrated in Fig. 10, both $z[i]$ and the inner product of M_r and M_i can reflect the difference for case (a), but only $z[i]$ is capable of indicating the difference for case (b) since M_r is parallel to M_i in this case, which amounts to cases where all grayscale values of pixels in M_r are equally scaled from M_i but nothing moves, or technically the static scenes where the light source is blinking.

Based on Eq. (A1), the evolution of $z[i]$ for an image sequence of a (2,0) mode is plotted against the frame ID i's in Fig. 11. From Fig. 11(a), the overall variation of $z[i]$, two complete cycles are identified, which gives $N_c = 2$. By zooming in as shown in Fig. 11(b), the position of this second notch is located at $N = 175$. Therefore for this image sequence, which is recorded with $f_s = 5000$ fps or 5000 Hz, the observed resonance frequency is

$$f_o = 5000 \times \frac{2}{175} = 57.14.$$

The driving frequency f_d for this example in Fig. 11 is 58 Hz, hence $f_o/f_d \approx 1$, which is consistent with the behaviors of all other zonal modes (cf. Fig. 4).

Notice that Eq. (3) in the main text provides a means of estimation and hence the result is not exact. Among the parameters, f_s is a controlled parameter and N_c is obtained from Fig. 11(a) with no ambiguity. Therefore any error is expected to contribute solely from the estimation of N. Notice that the frame ID i's are discrete and despite the observed minimal difference at $i = 175$, the exact minimal difference may correspond to any instant between those when frames $i = 174$ and 176 are captured. In other words, a maximal under- or overestimation of one frame for N is expected. With regard to the experimental setup aiming at recording at least 20 frames per cycle of oscillation and a total of 200 frames for each image sequence, the result of a preliminary error estimation is obtained as shown in Table III, where $N_{\max}$ and $N_{\min}$ are the maximal and minimal number of frames per cycle of oscillation possible given an N_c, and N_r is the remaining frames of images not counted within the N_c cycles. The error estimates ε are defined as

$$\begin{aligned} \varepsilon_{\max\pm} &= \left| \frac{1}{N_{\max}} - \frac{1}{N_{\max} \pm 1} \right|, \\ \varepsilon_{\min\pm} &= \left| \frac{1}{N_{\min}} - \frac{1}{N_{\min} \pm 1} \right|, \end{aligned} \tag{A2}$$

and therefore are the estimates of error per single frame of over- or underestimating N. For virtually all experiments, $N_c \leqslant 10$ and $N_{\max}$ and $N_{\min}$ depend on each particular mode produced by different driving frequencies. According

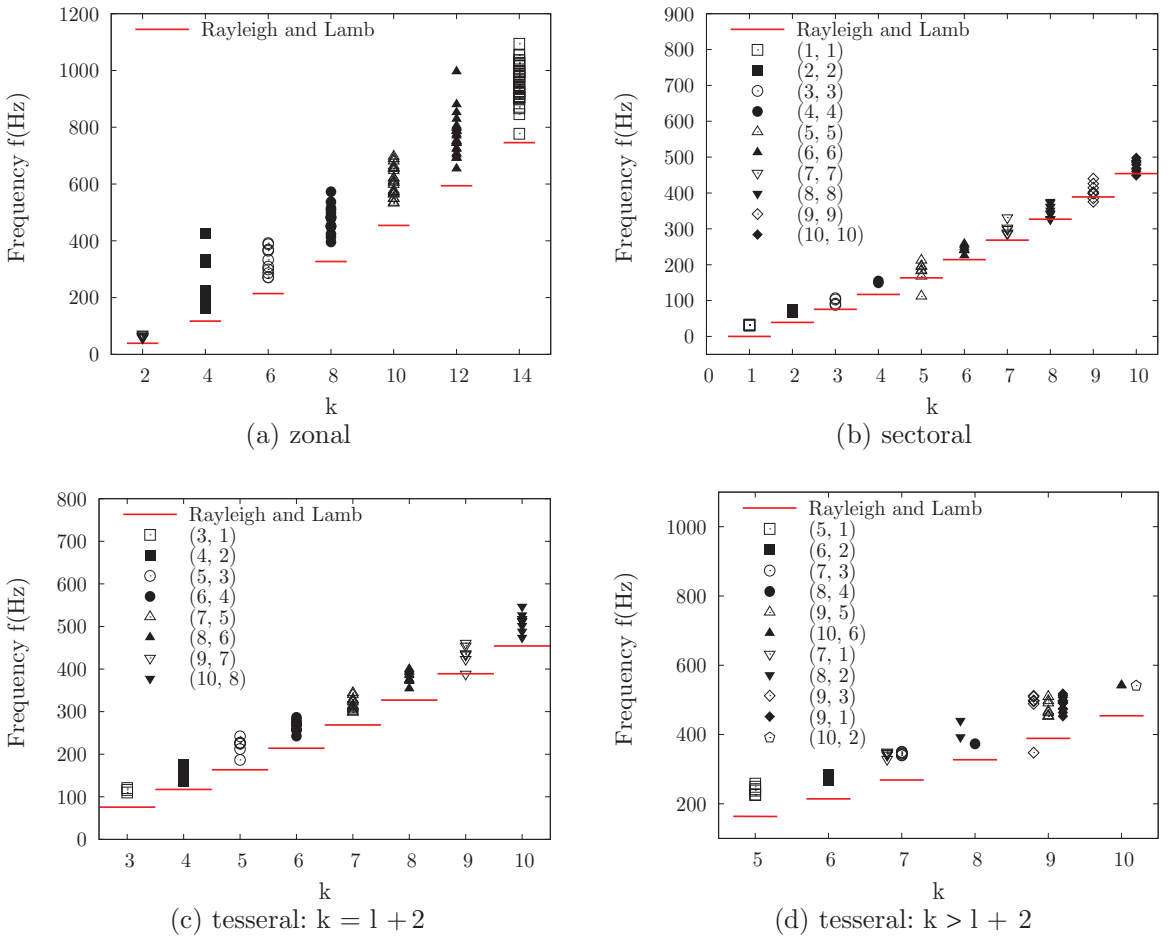

FIG. 13. (Color online) Direct comparison of experimental data with the Rayleigh and Lamb theory according to Eq. (5). The comparison yields a uniform underestimation by the theory.

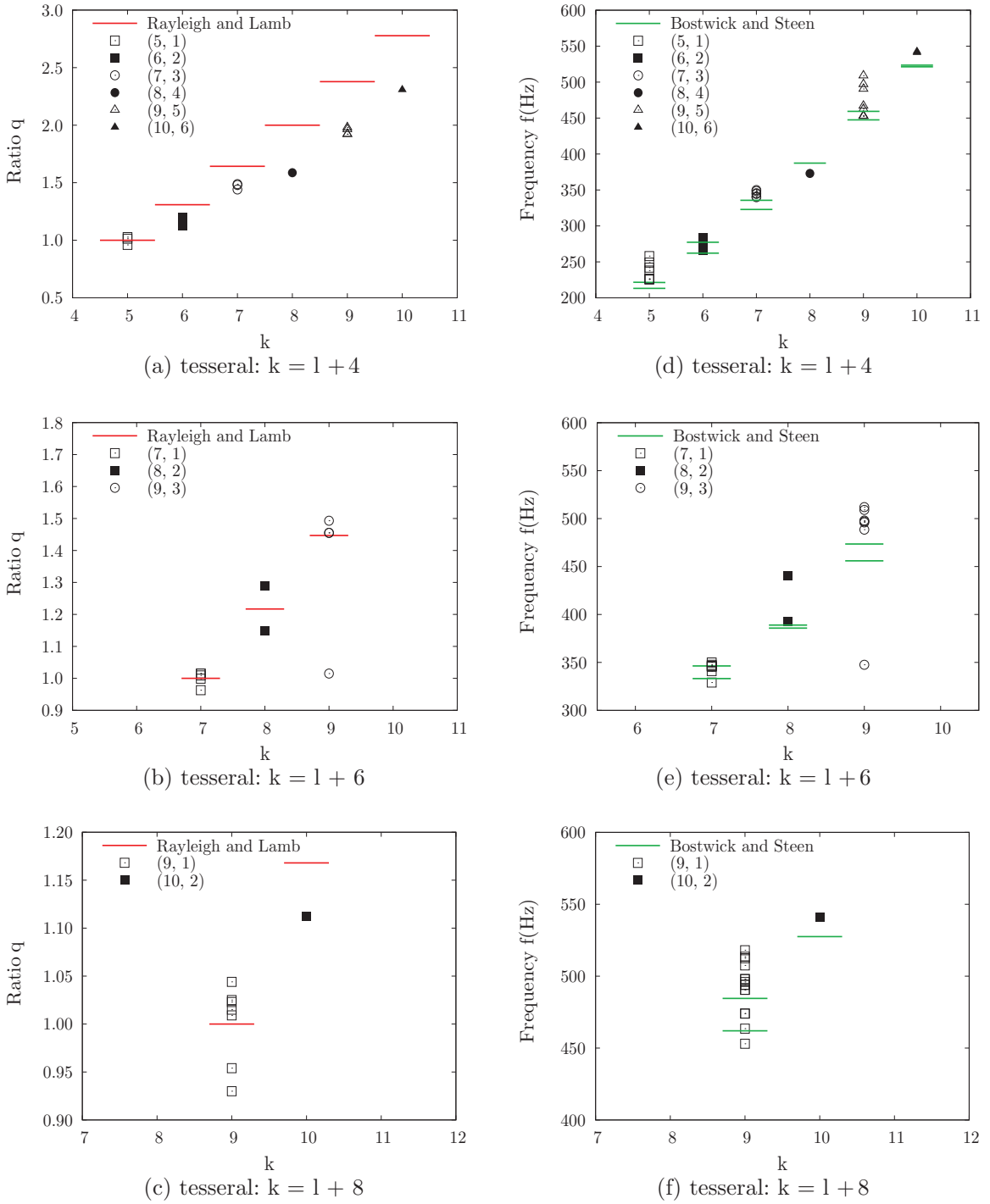

FIG. 14. (Color online) Additional results of comparing experimental data to theories: (a)–(c) comparison with the Rayleigh and Lamb theory using the normalized scheme; (d)–(f) direct comparison to the Bostwick and Steen theory.

to Table II, the estimated resonance frequencies possess a precision of approximately 3%.

4. Detailed comparison of driving and observed frequencies for all observed modes

For all observed modes, the ratios f_o/f_d of the estimated resonance frequencies (f_o) to the driving frequencies (f_d) are plotted against the driving frequencies in Fig. 12(a) for all observed zonal modes, Fig. 12(b) for sectoral modes, and Figs. 12(c) and 12(d) for tesseral modes. In Fig. 12(a), ratios of the frequencies are all equal to 1 with virtually undetectable deviation. For sectoral and tesseral modes, however, the ratios are equal to 0.5.

5. Direct comparison of experimental data with theories

The results of directly comparing experimental data with theory based on Eq. (5) are presented in Fig. 13. For all observed modes, theoretical predictions uniformly

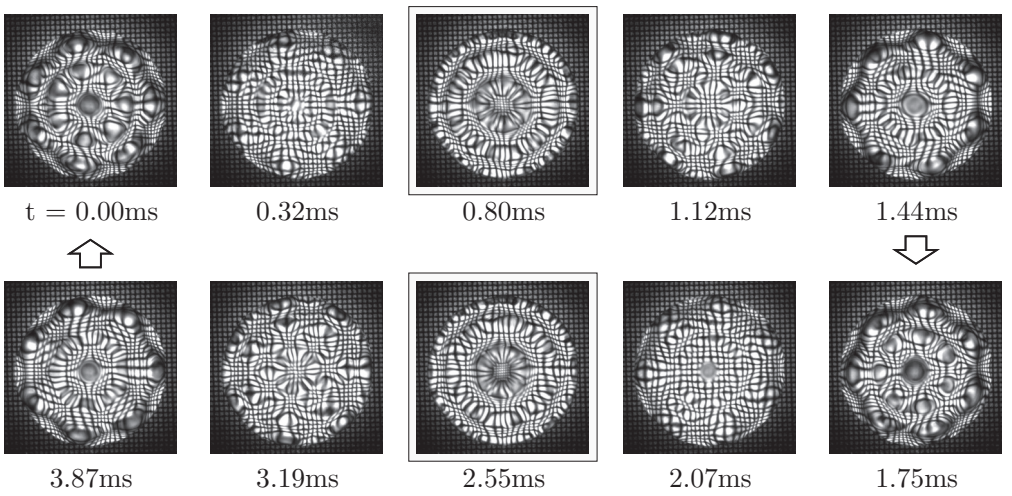

FIG. 15. Image sequence of a $(k,l) = (7,7)$ mode mixing with a $(k,l) = (10,0)$. The latter appears twice in one period of the former and oscillates with the same frequency as the driving signal, and hence is boxed to highlight. The shape is confirmed by comparing the boxed images to that of $(n,l) = (6,0)$ in Fig. 5, as the former possess the same number (=3) of circular regions where the mesh pattern is magnified (peaks) as the pattern is miniaturized (troughs) in the latter.

underestimate the resonance frequencies. Therefore we conclude from Fig. 13 that the Rayleigh and Lamb theory is insufficient for model behaviors of sessile drops.

6. Additional results of comparing experimental results with theories

Results of comparing resonance frequencies of tesseral modes (those not shown in Fig. 6) with predictions by the Rayleigh and Lamb and Bostwick and Steen theories are presented in Fig. 14. For tesseral modes with $k = l + 4$, which are physically the modes with three layers of azimuthal wave patterns, the same overshooting trend by the Rayleigh and Lamb theory is obvious from Fig. 14(a), while a reasonable match exists between experimental data and predictions by the Bostwick and Steen theory. For tesseral modes with $k = l + 6$ and $k = l + 8$, a conclusion of how well the experiment and theory match one another is more difficult to draw, since technically these modes are much more difficult to generate and observe in experiments, which limits the number of observations and the amount of data available for comparing with the theories.

7. Additional mode-mixing examples

In Fig. 15, most images exhibit a heptagonal wave pattern of one single layer, and therefore a (7,7) mode is identified. Those of $t = 0.80$ and 2.55 ms clearly show axisymmetric patterns, and the corresponding zonal mode is (10,0). Therefore, Fig. 15 demonstrates an example of a sectoral of (7,7) mixing with a (10,0) zonal mode.

The image sequence in Fig. 16 shows another example of mode mixing. For images of $t = 0.88$ and 2.26 ms, similar zonal patterns corresponding to the (12,0) mode are identified. Since other images all exhibit a hexagonal star confined within a hexagon, a component of the (8,6) mode is recognized. Therefore Fig. 16 is an example of a tesseral (8,6) mixing with a zonal (12,0) mode.

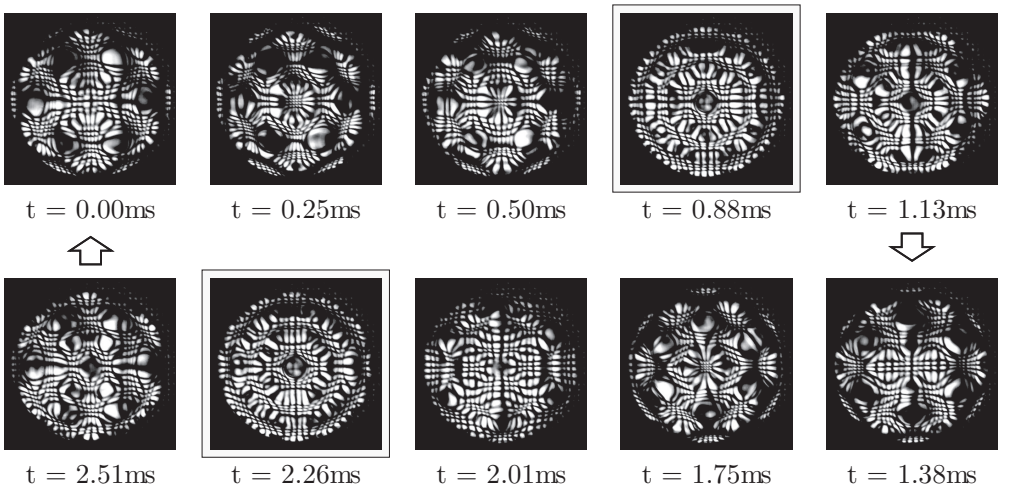

FIG. 16. Image sequence of a $(k,l) = (8,6)$ mode mixing with a $(k,l) = (12,0)$. The latter is boxed for the same reason as the (10,0) in Fig. 15. The shape is confirmed by comparing the boxed images to that of $(n,l) = (7,0)$ in Fig. 5.

[1] L. Rayleigh, Proc. R. Soc. London **29**, 71 (1879).
[2] H. Lamb, *Hydrodynamics* (Cambridge University Press, Cambridge, UK, 1932).
[3] W. Thompson, in *Mathematical and Physical Papers* (Cambridge University Press, Cambridge, UK, 1890), pp. 384–386.
[4] E. Trinh, A. Zwern, and T. G. Wang, J. Fluid Mech. **115**, 453 (1982).
[5] T. G. Wang, A. V. Anilkumar, and C. P. Lee, J. Fluid Mech. **308**, 1 (1996).
[6] R. J. A. Hill and L. Eaves, Phys. Rev. E **81**, 056312 (2010).
[7] P. Brunet and J. H. Snoeijer, Eur. Phys. J. Spec. Top. **192**, 207 (2011).
[8] M. Strani and F. Sabetta, J. Fluid Mech. **141**, 233 (1984).
[9] S. Daniel, M. K. Chaudhury, and P.-G. de Gennes, Langmuir **21**, 4240 (2005).
[10] L. Dong, A. Chaudhury, and M. K. Chaudhury, Eur. Phys. J. E **21**, 231 (2006).
[11] X. Noblin, R. Kofman, and F. Celestini, Phys. Rev. Lett. **102**, 194504 (2009).
[12] N. A. Chebel, F. Risso, and O. Masbernat, Phys. Fluids **23**, 102104 (2011).
[13] S. Dorbolo, D. Terwagne, N. Vandewalle, and T. Gilet, New J. Phys. **10**, 113021 (2008).
[14] N. Yoshiyasu, K. Matsuda, and R. Takaki, J. Phys. Soc. Jpn. **65**, 2068 (1996).
[15] M. Perez, Y. Brechet, L. Salvo, M. Papoular, and M. Suery, Europhys. Lett. **47**, 189 (1999).
[16] J. S. Sharp, D. J. Farmer, and J. Kelly, Langmuir **27**, 9367 (2011).
[17] S. Chandrasekhar, *Hydrodynamic and Hydromagnetic Stability* (Oxford University Press, New York, 1961).
[18] C. L. Shen, W. J. Xie, and B. Wei, Phys. Rev. E **81**, 046305 (2010).
[19] H. Azuma and S. Yoshihara, J. Fluid Mech. **393**, 309 (1999).
[20] M. Strani and F. Sabetta, J. Fluid Mech. **189**, 397 (1988).
[21] C. Bisch, A. Lasek, and H. Rodot, J. Mec. Theor. Appl. **1**, 165 (1982).
[22] H. Rodot and C. Bisch, *European Symposium on Material Sciences under Microgravity, 1984*, Paper ESA SP-222, p. 23 (unpublished).
[23] J. B. Bostwick and P. H. Steen, J. Fluid Mech. **714**, 312 (2013).
[24] J. B. Bostwick and P. H. Steen, J. Fluid Mech. **714**, 336 (2013).
[25] J. B. Bostwick and P. H. Steen, Phys. Fluids **21**, 032108 (2009).
[26] S. Ramalingam, D. Ramkrishna, and O. A. Basaran, Phys. Fluids **24**, 082102 (2012).
[27] R. W. Smithwick and J. A. M. Boulet, J. Colloid Interface Sci. **130**, 588 (1989).
[28] A. Ganan and A. Barerro, Microgravity Sci. Technol. **3**, 70 (1990).
[29] D. V. Lyubimov, T. P. Lyubimova, and S. V. Shklyaev, Phys. Fluids **18**, 012101 (2006).
[30] D. V. Lyubimov, T. P. Lyubimova, and S. V. Shklyaev, Fluid Dyn. **39**, 851 (2003).
[31] I. S. Fayzrakhmanova and A. V. Straube, Phys. Fluids **21**, 072104 (2009).
[32] X. Noblin, A. Buguin, and F. Brochard-Wyart, Eur. Phys. J. E **14**, 395 (2004).
[33] S. Mettu and M. K. Chaudhury, Langmuir **28**, 14100 (2012).
[34] X. Noblin, A. Buguin, and F. Brochard-Wyart, Eur. Phys. J. Spec. Top. **166**, 7 (2009).
[35] R. W. Smithwick and D. M. Hembree, Jr., J. Colloid Interface Sci. **140**, 57 (1990).
[36] P. Brunet, J. Eggers, and R. D. Deegan, Phys. Rev. Lett. **99**, 144501 (2007).
[37] B. Vukasinovic, M. K. Smith, and A. Gleazer, J. Fluid Mech. **587**, 395 (2007).
[38] See Supplemental Material at http://link.aps.org/supplemental/10.1103/PhysRevE.88.023015 for video files of drop modes and look-up table.
[39] A. Ludu, *Nonlinear Waves and Solitons on Contours and Closed Surfaces*, 2nd ed. (Springer-Verlag, Heidelberg, 2012).